Journal of Biomedical Optics

SPIEDigitalLibrary.org/jbo

Robot-assisted three-dimensional registration for cochlear implant surgery using a common-path swept-source optical coherence tomography probe

Saumya S. Gurbani
Paul Wilkening
Mingtao Zhao
Berk Gonenc
Gyeong Woo Cheon
Iulian I. Iordachita
Wade Chien
Russell H. Taylor
John K. Niparko
Jin U. Kang

SPIE

Robot-assisted three-dimensional registration for cochlear implant surgery using a common-path swept-source optical coherence tomography probe

Saumya S. Gurbani,[a,*] Paul Wilkening,[a] Mingtao Zhao,[a] Berk Gonenc,[a] Gyeong Woo Cheon,[a] Iulian I. Iordachita,[a] Wade Chien,[b] Russell H. Taylor,[a] John K. Niparko,[c] and Jin U. Kang[a]
[a]Johns Hopkins University, Whiting School of Engineering, 3400 North Charles Street, Baltimore, Maryland 21218
[b]Johns Hopkins University, Department of Otolaryngology-Head and Neck Surgery, 601 North Caroline Street, Baltimore, Maryland 21287
[c]University of Southern California, Department of Otolaryngology-Head and Neck Surgery, 1520 San Pablo Street, Suite 4600, Los Angeles, California 90033

Abstract. Cochlear implantation offers the potential to restore sensitive hearing in patients with severe to profound deafness. However, surgical placement of the electrode array within the cochlea can produce trauma to sensorineural components, particularly if the initial turn of the cochlea is not successfully navigated as the array is advanced. In this work, we present a robot-mounted common-path swept-source optical coherence tomography endoscopic platform for three-dimensional (3-D) optical coherence tomography (OCT) registration and preoperative surgical planning for cochlear implant surgery. The platform is composed of a common-path 600-μm diameter fiber optic rotary probe attached to a five degrees of freedom robot capable of 1 μm precision movement. The system is tested on a dry fixed *ex vivo* human temporal bone, and we demonstrate the feasibility of a 3-D OCT registration of the cochlea to accurately describe the spatial and angular profiles of the canal formed by the scala tympani into the first cochlear turn. [DOI: 10.1117/1.JBO.19.5.057004]

Keywords: fiber optics imaging; imaging systems; endoscopy; optical coherence tomography; registration.

Paper 130886RR received Dec. 16, 2013; revised manuscript received Apr. 7, 2014; accepted for publication Apr. 8, 2014; published online May 7, 2014.

1 Introduction

Cochlear implant surgery is an elective procedure capable of restoring auditory sensing capability in patients with profound to severe hearing loss.[1–4] In patients presenting with profound hearing loss due to damaged or absent cochlear hair cells, implantation of a multichannel array aims to restore hearing by directly stimulating residual fibers of the auditory nerve via current injection, thus bypassing nonfunctional hair cells. Surgical opening of the cochlea adjacent to the round window, forming the cochleostomy, enables placement of an electrode into the scala tympani. Figure 1(a) depicts the cochleostomy site in a human temporal bone with the round and oval windows. An electrode array placed within the scala tympani stimulates auditory neurons to carry afferent traffic to the auditory brain stem. The electrode is coupled to an internal processor that is linked to an external microphone and speech processor to convert sound into electrical impulses carried by the electrode array. Figure 1(b) shows a drawing of the anatomy of the cochlea, highlighting the features relevant to cochlear implant surgery.

Cochlear anatomy creates an environment which requires extreme precision to avert cochlear damage.[5,6] The scala tympani is angulated in its proximal origin[7] and tapers from 2 to 3 mm at the round window to <1 mm at the basal turn, where the implant is placed. The scala tympani compartment is bounded by a thin basilar membrane cephalically and forms the foundation for the organ of corti. The basilar membrane is tethered to the osseous spiral lamina housing peripheral extensions of the auditory nerves. The intrascalar distance from the round window to the initial curvature of the basal turn is on average 6 to 7 mm in adults.[8] Preoperative planning to find the optimal insertion path for the electrode is important for proper electrode placement, particularly given risks to the basilar membrane with buckling or misdirection of the electrode array as it is advanced through the basal turn.[9]

Current standards of care involve computed tomography (CT) or magnetic resonance (MR) imaging to image cochlear anatomy. However, these modalities do not have sufficient resolution to generate a detailed image of the cochlea and, in the case of CT, the imaging procedure induces a dosage of radiation in the patient. In addition to path planning, preoperative imaging is necessary to determine if there are anomalies to be resolved prior to the surgery. CT and MR imaging cannot easily detect if a patient presents with an obliterated cochlea, wherein access to the basal turn is blocked by bone or fibrous tissue, and additional surgical drilling is needed to gain access to the cochlea.[10] Proper anatomical information of a patient's temporal bone can reduce complications arising from improper insertion trajectory or electrode placement. Such complications include damage to the spiral ligament, facial nerve exposure, dura exposure, damage to the chorda tympani, and long-term bacterial

*Address all correspondence to: Saumya Gurbani, E-mail: sgurbani@jhu.edu

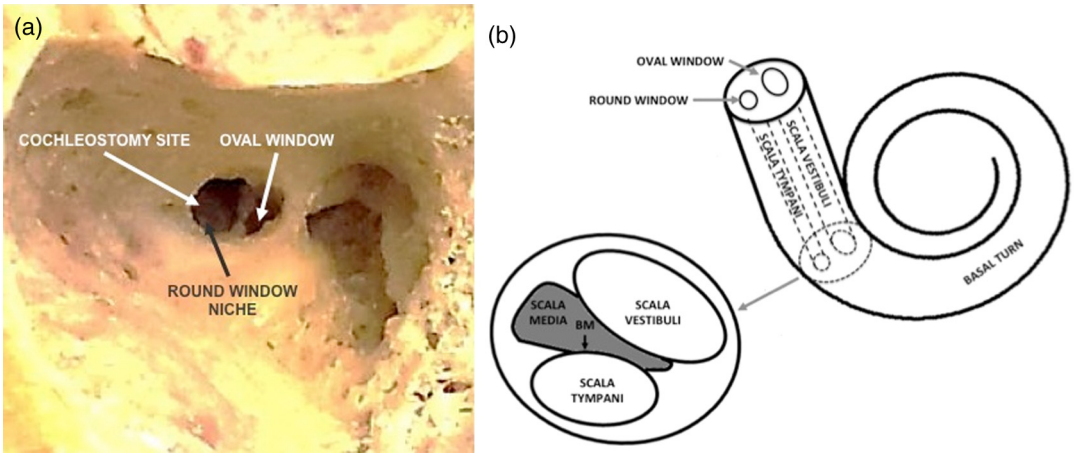

Fig. 1 (a) Cadaveric temporal bone dissection demonstrating the transmastoid, transfacial recess view of the round and oval windows of the cochlea. The oval windows position is superior to the round window niche. The site of cochlear opening is demonstrated in the anteroinferior aspect of the round window niche. The cochleostomy is positioned to avoid impaling the structures that separate the scala tympani from the more-cephalad scala media. (b) Schematic of the cochlear canal from the entrance to the first basal turn. The electrode is embedded in the scala typani at the basal turn to stimulate the auditory nerve cells at the basilar membrane (BM).

infection.[11–13] A 2004 study of 300 pediatric patients, an important population for the procedure, showed major complications occuring in 2.3% of patients and minor complications in 16%.[14]

Recent research into cochlear implant surgery assistance has ranged from developing novel piezoresistive-sensing electrodes to patient-customized drill guides.[15,16] In this work, we focus on a three-dimensional (3-D) optical coherence tomography (OCT) image registration to navigate scala tympani anatomy and plan the surgical procedure. OCT is an ideal modality for this aim as it uses biologically safe infrared light and is capable of producing high-resolution 3-D images of biological tissue.[17–19] With specific regard to cochlear implant surgery, OCT has been shown to be a useful modality for preoperative image registration. Research groups have used a Michelson-interferometer OCT setup for imaging the cochlear lumen to determine its orientation presurgically[20] and for external imaging of the cochlear canal through the cochlear promontory.[21] Lin et al.[22] demonstrated rapid *in vivo* lumenal imaging of murine cochleae using a rotating 350-μm distal OCT probe, signifying the potential of real-time catheter-based probes for otologic interventions.

In this work, we seek to demonstrate the use of a common-path catheter-based OCT probe guided by a surgical robot for 3-D image registration. Common-path OCT provides advantages over traditional Michelson-based setups,[23] especially in a surgical setting. A small optical fiber probe is capable of entering the cochlear lumen through surgical entry points. With a single arm, the probe functions as a highly accurate distance sensor. No additional alignment is required and consequently catheter probes can be quickly exchanged between surgeries. An inexpensive, disposable common path probe could serve as a surgeon-held navigational tool in cochlear implant surgery. We present a robot-mounted common-path swept-source OCT (CP-SSOCT)-based fiber endomicroscope capable of imaging the cochlear canal and guiding surgeons to the basal turn. To the best of our knowledge, this is the first time that 3-D image registration using a common path catheter probe guided by a surgical robot has been employed for cochlear implant surgery. We demonstrate the use of this system in dry *ex vivo* human temporal bones to show a proof-of-concept for future *in vivo* surgical planning and intraoperative guidance.

2 Materials and Methods

2.1 *Optical System Setup*

We use a CP-SSOCT because it yields many benefits in a surgical setting.[24] The ability to use a lensless fiber system yields small imaging probes, which are capable of being used in the restricted environment of the cochlear canal. Because probes must be sterile for each operation, a single-optical arm is beneficial. Furthermore, negating the additional alignment of a reference arm and the low cost of polished fiber allows the probes to be disposable between surgical procedures. Additionally, the single-arm setup of CP-SSOCT prevents the formation of complex-conjugate images of target tissue, allowing for simplified image processing. The main advantage of the common-path setup is that it allows accurate distal measurements relative to the probe tip, allowing highly accurate image registration. A schematic of our CP-SSOCT system is

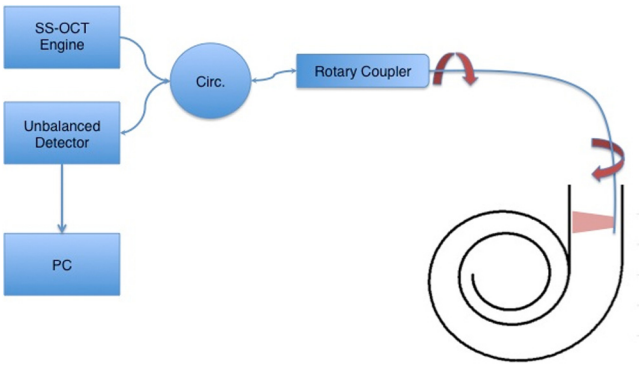

Fig. 2 Schematic of common-path swept-source optical coherence tomography (CP-SSOCT) system with a side-viewing rotary probe. The system has the ability to run in either standard or common path configurations, though the latter is chosen for this work.

shown in Fig. 2. The system is built to have the ability to run in both standard and common-path configurations, though the latter is chosen for this work to allow for multiple experiments during a single session.[25] The OCT engine is a 1310-nm swept-source laser (Axsun Technologies, Inc., Billerica, Massachusetts) operating at a 50-kHz A-scan rate with a 19-μm axial resolution. Return signal is collected using a single input on a balanced amplified photodetector (ThorLabs, Inc., PDB110C, Newton, New Jersey) and digitized (Alazar ATS9350, Pointe-Claire, Quebec, Canada). Output light is passed through an SC-connector rotary coupler (Princetel, Inc., Hamilton, New Jersey), which is rotated at 5 to 10 Hz. The distal fiber is SMF-28 (Gould Technology LLC, Millersville, Maryland) with a buffered diameter of 250 μm and a cladding diameter of 125 μm. In order to image "sideways," perpendicular to the fiber axis, the fiber is polished to a 45-deg angle[26] using an aluminum oxide fiber-optic polishing system (KrellTech, Morganville, New Jersey). Similar sideviewing schemes involving polishing, microprisms, and fused half-ball lenses have been previously used by many groups.[27–31] In order to maintain a single-arm setup and to keep the probe simple for disposability, a bare-polished fiber is selected. Although this lensless system cannot focus light at the distal end of the probe, the reflected signal provides sufficient signal-to-noise ratio (SNR) for imaging. To confirm the imaging capability of the bare sideview probe, the SNR is calculated at various distances by translating a mirror from 0.5 to 3 mm. The overlaid A-scans are shown in Fig. 3. The SNR decays from 50 dB at 0.5 mm to 30 dB at 3 mm, a sufficient distance given the small diameter of the cochlear canal. The return interference signal from the OCT probe is passed through the circulator to an unbalanced detector, from where it is digitized and processed in custom C++ software.

The reference plane for the interferometer comes from the cylindrical side of the bare fiber as a result of the Fresnel reflection from the polished surface. The reference level is highly sensitive to the angle of polish. Sharma and Kang[28] showed the exponential decay of reference power at the side of the fiber from ~1% when polished at 45 deg to nearly 0% at 50 deg due to the imperfect coupling back into the fiber core. Analysis of the profile of coupling is calculated using ABCD matrix theory for a beam passing through a cylindrical lens.[32] With, relative to the fiber axis, x representing the curved transverse plane, y representing the noncurved transverse plane, and z representing the plane along the fiber axis, the electric field of the recoupled beam is calculated to be

$$E(x,y,z) = E_0 \frac{\omega_0}{\sqrt{\omega_x(z)\omega_y(z)}} e^{-i\frac{k}{2q_x(z)}x^2} e^{-i\frac{k}{2q_y(z)}y^2} \gamma(z_{\text{forward}}), \tag{1}$$

$$\gamma(z_{\text{forward}}) = e^{-i\left\{kz - 0.5\tan^{-1}\left[\frac{\lambda_0 f}{\pi\omega^2(z_{\text{forward}})1+fM(z)}\right] - 0.5\tan^{-1}\left[\frac{\lambda_0}{\pi\omega^2(z_{\text{forward}})M(z)}\right]\right\}}, \tag{2}$$

where E_0 is the maximum amplitude of the electric field, ω_0 is the mode field diameter of the fiber, k is the wave number of light, $M(z) = [1/R(z) + (1/z) + (1/f)]$, $R(z)$ is the radius of curvature, f is the focal length of the cylindrical lens, and z_{forward} is the distance the beam travels between the core and the cladding-air interface on the side of the fiber. Figure 4(a) shows a ray trace of the beam as it reflects off of the cylindrical surface dependent on the polish angle. Polishing at nonperpendicular angles produces imperfect recoupling into the fiber core. Due to the cylindrical nature of the fiber, some astigmatism occurs and increases with off-angle polishing. Using Eq. (1), the eccentricity of the beam re-entering the fiber core is calculated to be 0.57 at 45 deg. Figure 4(b) shows a schematic of the astigmatism of the reflected light, producing some additional coupling loss into the fiber core. A 45-deg polish allows for

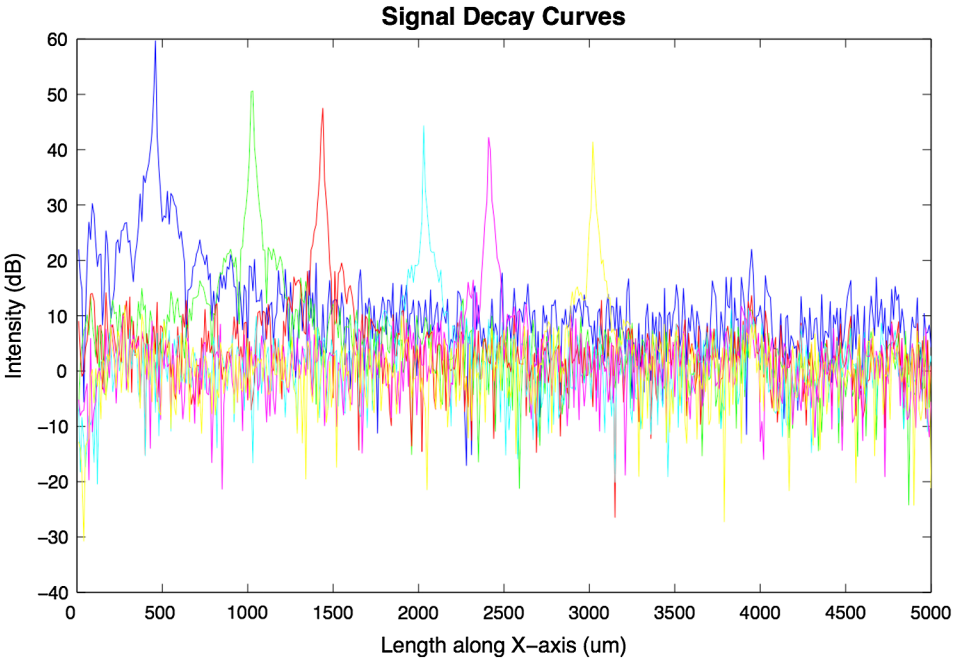

Fig. 3 Signal decay profile of a bare-fiber probe polished at 45 deg. A-scan signals from a mirror surface showing the signal-to-noise ratio decay from 50 to 30 dB by translating the mirror from 0.5 to 3 mm.

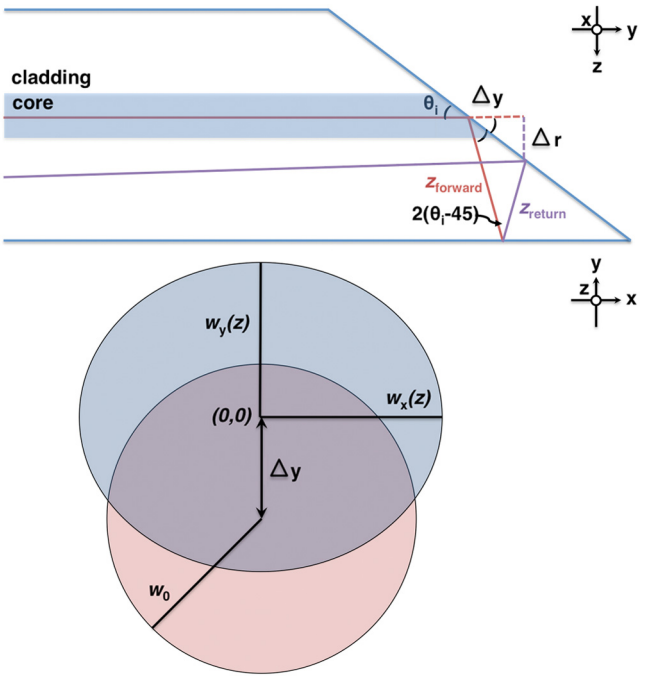

Fig. 4 Coupling loss of reflected light back into the fiber core is imperfect with a sideviewing probe, due to polish angle and astigmatism. (a) Ray trace of the incident (red) and return (purple) beams showing beam deflection away from the core based on polish angle, and (b) astigmatism due to the focusing of light by the cylindrical surface of the SMF causes additional recoupling loss.

sufficient reflected power to generate a reference signal while minimizing astigmatism. The Axsun laser has an average output power of 20 mW, which yields an average of 10 mW at the probe tip. Measured reflectance powers from the sideview probe polished at 45 deg were 22 ± 12 μW. Accounting for the return loss through the 50–50 coupler, this yields a reflectance power of 0.4%. The deviation from the theoretical 1% can be accounted for by imperfections in fiber polishing and the slight angular torque exerted on the fiber by the polishing pad. During fabrication, the probe was polished while monitoring the CP-OCT signal for a clear single-sinusoidal modulation.

The fiber is placed inside a 25-gauge (25G) hypodermic tube (McMaster-Carr, Atlanta, Georgia) with a window cut into the side to allow the beam to exit. The proximal fiber is glued using UV curable epoxy to the needle, providing mechanical support and smooth transmission of angular torque to the fiber when connected to the rotary coupler. A 600-μm outer diameter polyimide sheath (Microlumen, Inc., Oldsmar, Florida) is placed over the needle. This sheath prevents tissue and dust from entering the needle and damaging the fiber optic probe. Due to its semitransparency in the near infrared range, the sheath allows the light to pass without significant attenuation. The distal end of the probe is sealed with epoxy. The distal end of the probe is ~20 cm long and 600 μm in diameter, which allows it to be small enough to pass up to the basal turn of the cochlear canal. Figure 5 shows a schematic and photograph of this sideviewing probe.

2.2 *Robot System*

Due to the small working area within the cochlea (6 to 7 mm in depth and down to <1 mm in diameter), it is crucial for surgeons

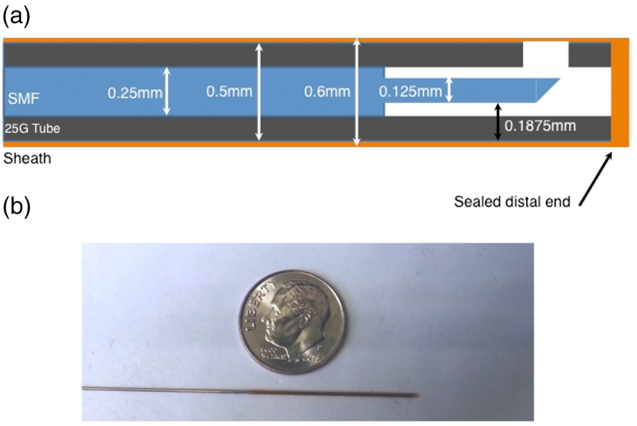

Fig. 5 (a) Schematic of the bare SMF, polished at 45 deg, encapsulated in a hypodermic needle and polyimide sheath. (b) Photograph of the 600-μm probe next to a US dime.

to precisely and accurately navigate the region of interest. Toward this aim, we incorporate the "EyeRobot2" platform developed by the Computer Integrated Surgical Systems and Technology Engineering Research Center (CISST ERC) at the Johns Hopkins University.[33] EyeRobot2 is a five degrees of freedom surgical robot to assist surgeons in various procedures; it has previously been used with vitreoretinal surgical tools, some of which are based on OCT.[34] The robot is capable of micrometer-scale precision movement of its surgical tool tip. The tool tip is attached to a handle with force-sensing capabilities. The robot is operated in cooperative mode, where the robot senses the forces exerted by the surgeon on the tool handle and moves the tool to comply. By mounting the rotary coupler to the robot arm, a sixth degree of freedom is gained. Figure 6(a) shows the setup of the probe mounted onto the EyeRobot2 platform. The rotary coupler is encapsulated in a custom-built case, which connects the coupler to a stepper motor (Maxon Precision Motors, Fall River, Massachusetts). This casing also tightly couples the proximal end of the hypodermic needle of the imaging probe with the motor. As a result, the motor, casing, and the entire length of the needle probe rotate smoothly and concurrently. Figure 6(b) shows a close up of the rotary arm of the robotic system attached to the needle probe. Video 1 shows the robot and mounted probe as set up during an experiment imaging a dry human temporal bone.

To reduce vibration, the needle probe is passed through two additional short 21G tubes proximal to the length of needle

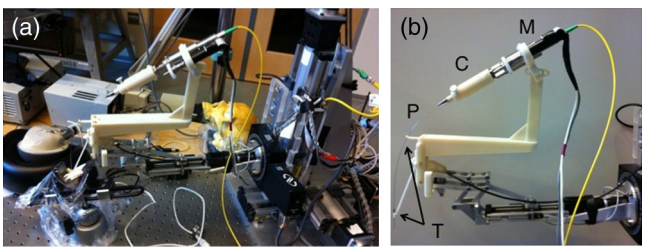

Fig. 6 (a) Photograph of the EyeRobot2 platform with the imaging probe mounted. (b) Close-up of the robot arm with the mounted rotary motor (M), custom-built casing (C), 21G tubes for restricting lateral motion (T), and CP-SSOCT needle probe (P). Video 1 (MOV, 8.58 MB) [URL: http://dx.doi.org/10.1117/1.JBO.19.5.057004.1] shows this setup being used in imaging a dry temporal bone.

which enters the temporal bone. These two tubes are affixed to the robotic arm, as shown in Fig. 6(b). These two tubes restrict the lateral movement of the needle probe as it rotates. Experimental calibration of the probe by imaging the inside of a smooth plastic cylinder showed the lateral vibrations were insignificant and on the order of the axial resolution of the probe.

2.3 *Imaging and Analysis*

The mounted probe was tested on a dry *ex vivo* human temporal bone. The probe is position to be approximately coaxial to the round window and is then passed through the round window aperture. The positioning and rotation of the probe are controlled by robotic software. Using the robot to restrict motion along the probe's axis, the probe is slowly navigated down the cochlear canal, taking rotary OCT scans at increments of 200 μm.

Software to acquire and analyze data is performed by using a hybrid CPU and graphics processing unit (GPU) system. The imaging software is synchronized with the motor controller such that the system collects A-scans concurrent with motor rotation, experimentally calculated to be accurate within 10 ms. A double buffer is used to store unprocessed A-scans to reduce any processing delays. Since the swept-source laser is free-running, a variable amount of A-scans may be collected during each synchronized rotation, but this minimizes the angular "twist" that could occur if the systems were unsynchronized. The GPU is used to perform a fast Fourier transform on spectra to produce the depth profile image for each A-scan. A-scans are averaged to produce 3072 scans per rotary image and then converted to radial display using a polar-to-cartesian algorithm with interpolation to obtain discrete pixels. Though the image is displayed at 512×512 pixels, 3072 scans are used to reduce aliasing during interpolation. Contours are calculated on these radial images using an edge detection algorithm. Contours are processed by the EyeRobot2 platform to generate a "virtual fixture" to restrict the motion of the probe, avoid collisions with the cochlear membranes, and maintain a coaxial configuration with the cochlear canal. Figure 7 shows the software workflow used to process, display, and analyze rotary images in real-time.

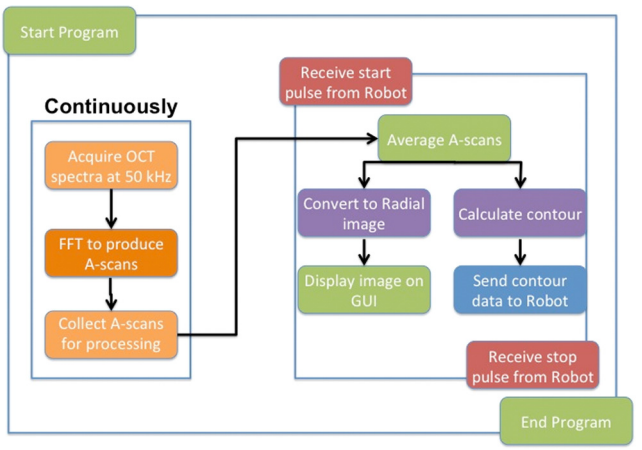

Fig. 7 Multithreaded workflow of the CP-SSOCT software system. CPU threads include the main (green), image processing (light orange), postprocessing (purple), and robot communication threads (red and blue). A GPU (dark orange) is used to perform the complex FFT operation.

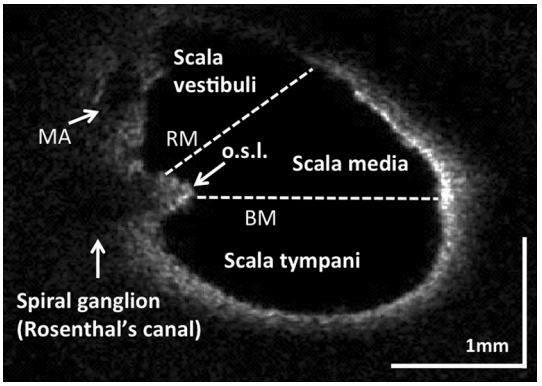

Fig. 8 A rotary scan depicting a cross section of a dry human temporal bone, with annotations overlain for relevant anatomy. Because the tissue has been removed during preparation, only bony structures are visible; the cavities for the modiolar artery (MA) and spiral ganglion (housed in Rosenthal's canal) are visible within the medial border of the cochlear canals. The location of the scala media, shown by dotted lines, is estimated based on the bony projection of the osseous spiral lamina (o.s.l.), bordered by Reissners membrane (RM) and the BM.

3 Results

A rotation scan was taken midway down the cochlear canal of a fixed, dry human temporal bone. The tissue from the bone was removed during the preparation process, leaving only the bony structures. Figure 8 depicts this scan, with the fiber and sheath reflections filtered out and with anatomical annotations overlain. The superior and inferior chambers of the cochlear canal are outlined, though the dividing scala media and membranes are removed. The osseous spiral lamina, a bony projection from the modiolus of the cochlea and a part of the structure dividing the two chambers, is visible. From this, we can estimate the location of the two membranes which form the scala media. Rosenthal's canal houses the spiral ganglion, the mass of neuron bodies receiving input at the hair cells, and is visible medial to the osseous spiral lamina. Just superior to that is a cavity formed by the modiolar artery, which perfuses the cochlea.

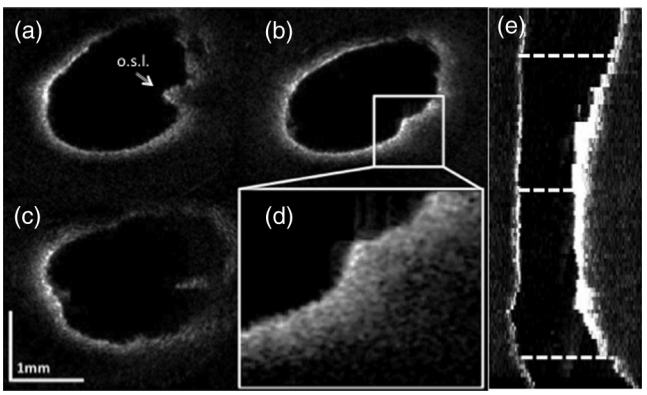

Fig. 9 Radial scans of the cochlear lumen (a) just below the round window (top-left), (b) in the middle of the canal (top-right), and (c) at the basal turn (bottom-left) indicate the orientation of the scala tympani and scala vestibuli. (d) A 1×1 mm^2 inset (bottom-right) demonstrates the ability of the probe to detect local anatomy. (e) A sagittal cross section of the three-dimensionl (3-D) data volume shows the curvature of the cochlear canal, with dotted lines depicting the locations of (a)–(c). The osseus spiral lamina (o.s.l.) is indicated in (a).

Selected images taken from a scan down the round window to the basal turn of a dry fixed human temporal bone are shown in Figs. 9(a)–9(c). The reflection from the surface of the fiber and the sheath are filtered out for display purposes. The lumen of the cochlea in these images shows the merged scala tympani and scala vestibuli (due to the removal of tissue when the bone is fixed). The diameter and orientation of the canal fluctuate as the probe progresses deeper. The probe is able to clearly detect the surface. In Fig. 9(d), a $1-1$ mm^2 inset taken from Fig. 9(b) shows the probe's ability to detect local anatomy. The rotation scans are stacked together to form a 3-D cube of data for the cochlear canal. A sagittal slice from near center of the data cube shows the trajectory of the cochlear canal from the round window to the first turn in Fig. 9(e). The width of the canal tapers from ~1.5 mm just inferior to the round window to <1 mm when approaching the first turn. The curvature of the first turn can be visualized in this cross section.

The combination of an OCT imaging probe with the EyeRobot2 platform allows for quantitative measurement of cochlear anatomy required for 3-D OCT image registration. After calibration, EyeRobot2 is capable of measuring the location of the distal end of the OCT probe with micrometer accuracy. To image the entire canal, the probe is positioned at the round window, parallel to the estimated axis of the cochlear canal, and then guided with robotic assistance stepwise down the length of the canal to the first basal turn. The probe is advanced at 200 μm down its axis at each step, A rotary scan is obtained, and a contour detection algorithm is applied to detect the walls of the canal. These contours serve a dual purpose: during the procedure, these contours allow the robot to recenter the probe to maintain coaxial descent down the canal and prevent trauma to the cochlear walls; after the procedure, these contours are processed to determine the orientation and shape of the cochlea. The location of the distal end was recorded by EyeRobot2 along with each rotary scan. 243 transverse rotary scans were obtained along the canal, until the probe reached the lateral wall of the first turn, traveling a total distance of 5.02 mm. The rotary scans were stacked together to form a 3-D image cube. Figure 10 shows this image from (a) an isometric angle and (b) down the lumen of the cochlear canal. Figure 10(c) shows a surface profile calculated from the contours. For image analysis, postprocessing of contours is done by filtering out segments in which a clear contour could not be detected (Video 2).

To validate that this 3-D registration model is anatomically correct, the angle of rotation of the basal turn is calculated based on the center axis of the canal. Using two piecewise orthogonal distance regression lines in the relatively straight segments of the canal proximal and distal to the start of the basal turn, the angle of the basal turn was calculated to be 37 deg. This angle of rotation for the proximal 5.02-mm segment down the canal is more acute than that shown previously with 3-D helico-spiral models of the human cochlea based on CT of fixed histopathologic specimens,[35] though this difference may be accounted for by anatomical variations, changes in the calculated curvature due to removal of soft tissue, and imaging only up to the first turn.

4 Discussion

Understanding preoperatively the anatomy of a patient is critical for mitigating risks of insertion trauma with cochlear implant

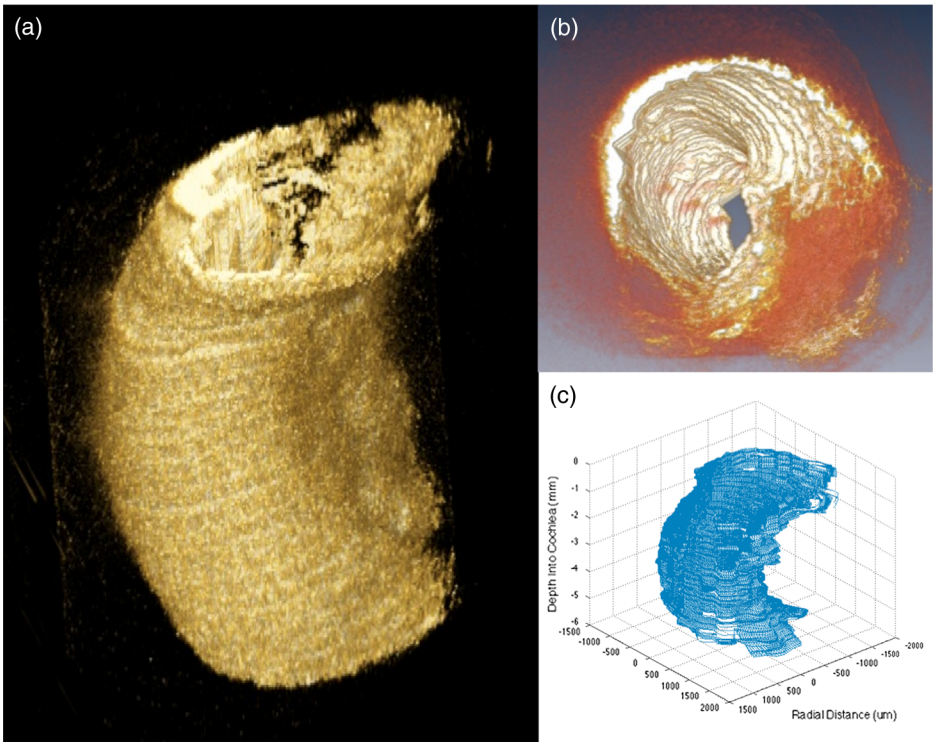

Fig. 10 (a) Isometric view of 3-D optical coherence tomography (OCT) volume of the cochlear canal. (b) Bird's eye view down the lumen of the cochlear canal. (c) Surface profile of the cochlear canal generated from the surface contours of the OCT scans taken at 200-μm intervals along the canal. Video 2 (MOV, 24.2 MB) [URL: http://dx.doi.org/10.1117/1.JBO.19.5.057004.2] shows postprocessing of contours to form 3-D surface profile.

surgery. In this work, we are able to demonstrate 3-D OCT registration using a sideviewing probe that is small enough to navigate into the luminal space of the cochlea to produce high-resolution images of the cochlea up to the first basal turn. Using the micrometer accuracy and precision of the EyeRobot2 platform, we are able to register the OCT images to the robot's frame and assist with navigation of the probe to generate accurate metric data of the canal structure and orientation The performance of our system was tested using a dry *ex vivo* dry fixed human temporal bone. Images of the cochlear canal in 3-D are produced along with quantitative spacial information, producing a personalized anatomical atlas of the target location of implant electrodes. These results suggest that a robot-assisted CP-SSOCT approach to preoperative planning and intraoperative guidance is feasible for cochlear implant surgery.

The quantification of OCT endoscopy images can have a meaningful impact on presurgical planning. Current standard of care involves estimating the angle of the basal turn through the use of sagittal CT cross-sections.[36] Lloyd et al.[37] discuss the use of 3-D modeling as a way to improve accuracy in presurgical planning, as compared with uniplanar measurements. The platform described in this article is able to apply this concept using OCT to quantify the angular profile of the scala tympani up to the first turn.

Recent advances in endoscopy, such as spectrally encoded endoscopy (SEE),[38] allow for quantified high-resolution surface profiles of anatomy by using spectral gratings. Kang et al.[39] have shown miniaturization of SEE probes to as small as 0.5 mm. However, OCT provides an additional advantage in that it allows for imaging of structures deep to the luminal surface, including arteries and nerves. Importantly, the location of the medial wall "spur" created by the osseous spiral lamina that houses critical neural structures is readily discernible with the techniques described here. As a tool to accurately detect critical boundaries of the scala tympani, CP-OCT offers a refined strategy of *in vivo* assessment of electrode array designs and surgical techniques aiming to place the array in proximity to neural targets without iatrogenic tissue injury.

A common-path approach to surgical use of OCT provides crucial clinical benefits. The stability of these probes from misalignment allows them to become disposable and robust enough to be easily integrated into a surgical workflow. Though the SNR and imaging depth are limited compared with lensed probes, for narrow surgical workspaces like the inner ear, common-path probes can be an excellent choice. In future work, we plan to investigate the use of a balanced detector for CP-OCT as implemented by Lorenser et al.,[40] to improve the probe's sensitivity.

This study has limitations that will be targeted in future work. With *in vivo* studies, the probe's performance in human tissue can be accurately measured. We tested the probe on a dry bone where the soft tisse was removed. An improved study could measure the effects of wet tissue on the probe's performance prior to an *in vivo* study. Furthermore, the current probe is only able to measure up to the first basal turn. With the use of a more flexible casing, the probe can be integrated with the electrode array. This would allow for real-time guidance during surgery, allowing the surgeon to negotiate cochlear turns with accuracy, averting contact and damage with the surrounding tissue. Improvement of distal optics, such as the use of a sapphire half-ball lens, could increase the sensitivity of the probe while maintaining a common-path configuration and small diameter. The implications of this probe are broad in both risk mitigation and improving the cost and efficiency of the surgical procedure. A combination of these two factors could ultimately lead to increased accessibility of cochlear implant surgery to the patient population.

5 Conclusion

To the best of our knowledge, this work demonstrates for the first time the feasibility of a robot-mounted CP-SSOCT imaging platform for 3-D image registration of the cochlear canal. The system is able to accurately measure the spatial and angular profiles of an *ex vivo* human temporal bone and locates important anatomical features. This platform has the potential to provide surgeons with preoperative guidance to ensure accurate insertion and atraumatic placement of the cochlear implant array.

Acknowledgments

The work reported here was funded in part by research support from Cochlear Americas and in part by Johns Hopkins University Internal Funds. Support of effort provided by the Sidgmore Family Foundation.

References

1. B. S. Wilson et al., "Better speech recognition with cochlear implants," *Nature* **352**(6332), 236–238 (1991).
2. H. J. McDermott, "Music perception with cochlear implants: a review," *Trends Amplif.* **8**(2), 49–82 (2004).
3. D. K. Ryugo, E. A. Kretzmer, and J. K. Niparko, "Restoration of auditory nerve synapses in cats by cochlear implants," *Science* **310**(5753), 1490–1492 (2005).
4. G. M. Clark, "The multiple-channel cochlear implant: the interface between sound and the central nervous system for hearing, speech, and language in deaf people a personal perspective," *Philos. Trans. R Soc. Lond. B Biol. Sci.* **361**(1469), 791–810 (2006).
5. O. Majdani et al., "A robot-guided minimally invasive approach for cochlear implant surgery: preliminary results of a temporal bone study," *Int. J. CARS* **4**(5), 475–486 (2009).
6. C. A. Todd, F. Naghdy, and M. J. Svehla, "Force application during cochlear implant insertion: an analysis for improvement of surgeon technique," *IEEE Trans. Biomed. Eng.* **54**(7), 1247–1255 (2007).
7. E. Erixon et al., "Variational anatomy of the human cochlea: implications for cochlear implantation," *Otol. Neurotol.* **30**(1), 14–22 (2009).
8. B. Escude et al., "The size of the cochlea and predictions of insertion depth angles for cochlear implant electrodes," *Audiol. Neurootol.* **11**(suppl 1), 27–33 (2006).
9. D. W. Kennedy, "Multichannel intracochlear electrodes: mechanism of insertion trauma," *Laryngoscope* **97**(5), 42–49 (1987).
10. V. Raut and J. G. Toner, "Cochlear implantation in the obliterated cochlea," *Clin. Otolaryngol.* **27**(3), 147–152 (2002).
11. H. G. Kempf, K. Johann, and T. Lenarz, "Complications in pediatric cochlear implant surgery," *Eur. Arch. Otorhinolarngol.* **256**(3), 128–132 (1999).
12. J. Reefhuis et al., "Risk of bacterial meningitis in children with cochlear implants," *N. Engl. J. Med.* **349**(5), 435–445 (2003).
13. K. R. Biernath et al., "Bacterial meningitis among children with cochlear implants beyond 24 months after implantation," *Pediatrics* **117**(2), 284–289 (2006).
14. K. Bhatia et al., "Surgical complications and their management in a series of 300 consecutive pediatric cochlear implantations," *Otol. Neurotol.* **25**(5), 730–739 (2004).
15. J. Wang and K. D. Wise, "A thin-film cochlear electrode array with integrated position sensing," *J. Microelectromech. Syst.* **18**(2), 385–395 (2009).
16. F. M. Warren et al., "Percutaneous cochlear access using bone-mounted, customized drill guides: demonstration of concept in vitro," *Otol. Neurotol.* **28**(3), 325–329 (2007).
17. D. Huang et al., "Optical coherence tomography," *Science* **254**(5035), 1178–1181 (1991).

18. E. A. Swanson et al., "In vivo retinal imaging by optical coherence tomography," *Opt. Lett.* **18**(21), 1864–1866 (1993).
19. R. Leitgeb et al., "Spectral measurement of absorption by spectroscopic frequency-domain optical coherence tomography," *Opt. Lett.* **25**(11), 820–822 (2000).
20. H. W. Pau et al., "Optical coherence tomography as an orientation guide in cochlear implant surgery?" *Acta Oto-Laryngologica* **127**(9), 907–913 (2007).
21. A. Sepehr et al., "Optical coherence tomography of the cochlea in the porcine model," *Laryngoscope* **118**(8), 1449–1451 (2008).
22. J. Lin, H. Staecker, and M. S. Jafri, "Optical coherence tomography imaging of the inner ear: a feasibility study with implications for cochlear implantation," *Ann. Otol. Rhinol. Laryngol.* **117**(5), 341–346 (2008).
23. U. Sharma, N. M. Fried, and J. U. Kang, "All-fiber common-path optical coherence tomography: sensitivity optimization and system analysis," *IEEE J. Sel. Top. Quantum Electron.* **11**(4), 799–805 (2005).
24. M. Zhao, Y. Huang, and J. U. Kang, "Sapphire ball lens-based fiber probe common-path optical coherence tomography and its applications in corneal and retinal imaging," *Opt. Lett.* **37**(23), 4835–4837 (2012).
25. M. Zhao et al., "Sensing and three-dimensional imaging of cochlea and surrounding temporal bone using swept source high-speed optical coherence tomography," *Proc. SPIE* **8571**, 857121 (2013).
26. D. Lorenser et al., "Ultrathin side-viewing needle probe for optical coherence tomography," *Opt. Lett.* **36**(19), 3894–3896 (2011).
27. A. M. Rollins et al., "Real-time in vivo imaging of human gastrointestinal ultrastructure by use of endoscopic optical coherence tomography with a novel efficient interferometer design," *Opt. Lett.* **24**(19), 1358–1360 (1999).
28. U. Sharma and J. U. Kang, "Common-path optical coherence tomography with side-viewing bare fiber probe for endoscopic optical coherence tomography," *Rev. Sci. Inst.* **78**, 113102 (2007).
29. D. C. Adler et al., "Three-dimensional endomicroscopy using optical coherence tomography," *Nat. Photonics* **1**, 709–716 (2007).
30. D. C. Adler et al., "Three-dimensional endomicroscopy of the human colon using optical coherence tomography," *Opt. Express* **17**(2), 784–796 (2009).
31. T.-H. Tsai et al., "Ultrahigh speed endoscopic optical coherence tomography using micro-motor imaging catheter and vcsel technology," *Proc. SPIE* **8671**, 1119–1132 (2013).
32. F. Bodem and H. D. Reidenbach, "Transformation of Gaussian beams by spherical and cylindrical lenses: the scalar diffraction approach," *Opt. Quantum Electron.* **8**(8), 207–211 (1976).
33. A. Uneri et al., "New steady-hand eye robot with micro-force sensing for vitreoretinal surgery," in *2010 3rd IEEE RAS and EMBS Int. Conf. on Biomedical Robotics and Biomechatronics*, pp. 814–819.
34. X. Liu et al., "Miniature fiber- optic force sensor based on low-coherence Fabry-Perot interferometry for vitreo- retinal microsurgery," *Biomed. Opt. Express* **3**(5), 1062–1076 (2012).
35. A. Kawano, H. L. Seldon, and G. M. Clark, "Computer-aided three dimensional reconstruction in human cochlear maps: measurement of the lengths of organ of corti, outer wall, inner wall, and Rosenthal's canal," *Ann. Otol. Rhinol. Laryngol.* **105**(9), 701–709 (1996).
36. H. W. Francis and S. Lloyd, "08:30: Cochlear rotation and cochlea implantation," *Otolaryng. Head Neck* **137**, 126–127 (2007).
37. S. K. W. Lloyd et al., "Developmental changes in cochlear orientation—implications for cochlear implantation," *Otol. Neurotol.* **31**(6), 902–907 (2010).
38. D. Yelin et al., "Three-dimensional miniature endoscopy," *Nature* **443**, 765 (2006).
39. D. Kang et al., "Miniature grating for spectrally-encoded endoscopy," *Lab Chip.* **13**, 1810–1816 (2013).
40. D. Lorenser et al., "Dual-modality needle probe for combined fluorescence imaging and three-dimensional optical coherence tomography," *Opt. Lett.* **38**(3), 266–268 (2013).

Saumya S. Gurbani received his MSE degree in biomedical engineering from Johns Hopkins University in 2013, where his research focused on OCT endoscopy in cochlear implant surgery. He is pursuing training as a physician-scientist with research focused on medical imaging.

Paul Wilkening received his BS in computer engineering and electrical engineering from Johns Hopkins University in 2011. He is currently a PhD candidate in computer science at Johns Hopkins University in his second year. He is conducting research on robot-assisted microsurgery under Dr. Russell H. Taylor with the Laboratory for Computational Sensing and Robotics.

Iulian I. Iordachita received his BEng, MEng, and PhD degrees in 1984, 1989, and 1996, respectively, all from the University of Craiova, Craiova, Romania. He is currently an assistant research professor in the Department of Mechanical Engineering and the Laboratory for Computational Sensing and Robotics, Johns Hopkins University, Baltimore, MD. His current research interests include medical robotics, medical instrumentation, smart surgical tools, computer assisted surgery and mechanisms and mechanical transmission of robots.

Russell H. Taylor received his PhD in computer science from Stanford in 1976. After spending 1976 to 1995 as a research staff member and research manager at IBM Research, he moved to Johns Hopkins University, where he is the John C. Malone Professor of Computer Science and director of the Laboratory for Computational Sensing and Robotics. He is the author of over 350 peer-reviewed publications and book chapters and has received numerous awards and honors.

John K. Niparko, MD, is the Tiber Alpert professor and chair of otolaryngology–head and neck surgery at the Keck School of Medicine of the USC. A native of Detroit, he received his zoology and MD training from the University of Michigan, where he completed his residency in otolaryngology and a fellowship in neurotology. He has authored more than 200 peer-reviewed reports and serves as editor-in-chief of *Otology & Neurotology*.

Jin U. Kang is Jacob Suter Jammer professor of the Department of Electrical and Computer Engineering at Johns Hopkins University. He received his PhD degrees from the School of Optics (CREOL) at the University of Central Florida in 1996. He has published more than 150 refereed journal papers. He is a fellow of the Optical Society of America, SPIE, and American Institute for Medical and Biological Engineering (AIMBE).

Biographies of the other authors are not available.